Journal of Materials Chemistry A

PAPER

View Article Online
View Journal | View Issue

Cite this: J. Mater. Chem. A, 2015, 3, 23930

Li-storage performance of binder-free and flexible iron fluoride@graphene cathodes†

Xuebo Hu,[a] Minhao Ma,[a] Rafael G. Mendes,[b] Mengqi Zeng,[a] Qin Zhang,[a] Yinghui Xue,[a] Tao Zhang,[a] Mark H. Rümmeli[b] and Lei Fu*[a]

Received 6th October 2015
Accepted 21st October 2015

DOI: 10.1039/c5ta08014b

www.rsc.org/MaterialsA

As flexible devices have become increasingly popular in our daily life, flexible energy-supply devices, especially flexible lithium-ion batteries (LIBs), have attracted great attention. Graphene foam is a lightweight, flexible and conductive interconnected network that can be directly used as a current collector material to disperse active materials. $FeF_3 \cdot 0.33H_2O$ is a suitable active cathode material with a high theoretical capacity and natural abundance. But its poor ionic and electrical conductivity limits its application. In order to combine the superior qualities of GF and $FeF_3 \cdot 0.33H_2O$, we developed a $scCO_2$-assisted method to grow $FeF_3 \cdot 0.33H_2O$ flower-like arrays perpendicularly on GF. Consequently, the designed composites efficiently combine the good flexibility of GF and high energy storage capacity of $FeF_3 \cdot 0.33H_2O$. The strong interaction between GF and $FeF_3 \cdot 0.33H_2O$ established by the $scCO_2$ method greatly improves the electron transport and ion migration. Thus, the obtained flexible electrode requires no binder, metal current collectors and conducting agents. It shows a capacity of about 145 mA h g^{-1} at a current density of 1C (200 mA g^{-1}) after assembled as a cathode electrode.

Introduction

Flexible devices have attracted extensive attention for various promising applications such as wearable sensors, touch screens, roll-up displays and implantable medical devices.[1–10] To fully realize flexible devices, the development of lightweight, and flexible energy-supply devices is urgently needed.[1–3] Among all the flexible energy-supply devices, flexible LIBs are attractive power sources of flexible electronic devices because of their high energy and power densities, high output voltage, long-term stability and environmentally friendly operation.[11,12] But the fabrication of flexible LIBs still presents enormous challenges on account of the lack of appropriate materials which have high electrical and/or ionic conductivities, large specific surface areas, and good chemical and electrochemical stabilities.[13–15]

The inherent outstanding mechanical and electronic properties of graphene make it an attractive material for applications in flexible energy devices.[2,16] The strong σ carbon–carbon bond endows graphene with a high Young's modulus and tensile strength.[17] The one-atom thick structure means graphene can easily deform in the direction normal to its surface, providing it with good flexibility so that it can be bent into arbitrary shapes without breaking.[2] Graphene also can be assembled into various macroscopic flexible materials, such as graphene papers,[18,19] and three-dimensional (3D) graphene porous networks.[16,20] In particular, graphene fabricated with a 3D structure such as graphene foam (GF) can serve as a current collector to directly disperse active materials without the requirement of a binder, as the binder might hinder the transfer of ions to the surface of the active materials and increases the polarization of the electrodes.[16] Moreover, GF is extremely light (*ca.* 0.65 mg cm^{-2}), which is lighter than the commonly used Cu (13 mg cm^{-2}) and Al (5 mg cm^{-2}) current collector material.[21–23] It also possesses an open pore system with a high porosity of ~99.7%,[16] through which electrolyte ions can easily access the graphene surface. Thus, this kind of graphene-based material can be directly used as binder-free electrode material for flexible LIBs.

To utilize flexible LIBs with higher capacity and power densities, iron fluoride ($FeF_3 \cdot 0.33H_2O$) has been chosen for its high theoretical capacity of 237 mA h g^{-1} ($1e^-$ transfer) and 712 mA h g^{-1} ($3e^-$ transfer), natural abundance and low cost.[24–30] But the application of it has been hindered by drawbacks such as slow diffusion of Li-ions and low electron conductivity. Constructing advanced nanostructures directly grown on a conducting substrate is one of the most promising routes to overcome these drawbacks. The supercritical carbon dioxide ($scCO_2$) method is an effective strategy to grow $FeF_3 \cdot 0.33H_2O$ on GF with a strong contact between them,[31,32]

[a]College of Chemistry and Molecular Science, Wuhan University, Wuhan, 430072, China. E-mail: leifu@whu.edu.cn

[b]IFW Dresden, P.O. Box 270116, 01069 Dresden, Germany

† Electronic supplementary information (ESI) available: The mass of the entire electrodes and the components, full XPS survey spectrum of FeF_3@GF–$scCO_2$, SEM images of GF and FeF_3@GF–HT, TEM image and EDX spectrum of FeF_3@GF–$scCO_2$, photograph of lighting a green LED device under various bending radii and directions, and galvanostatic charge/discharge voltage profiles of GF. See DOI: 10.1039/c5ta08014b

as the interface between the GF and $FeF_3 \cdot 0.33H_2O$ has an important impact on the electron transport and ion migration. With the help of the $scCO_2$ route, the designed composites can efficiently combine the good flexibility as well as high electrical conductivity of GF and high energy storage capacity of $FeF_3 \cdot 0.33H_2O$. Therefore, we developed a $scCO_2$ method to grow $FeF_3 \cdot 0.33H_2O$ flower-like arrays perpendicular to the surface of GF (denoted as FeF_3@GF–$scCO_2$). The GF network serves as both a highly conductive pathway for electrons and ions and a 3D interconnected flexible current collector. The 3D structure of flower-like $FeF_3 \cdot 0.33H_2O$ and GF has a large specific surface area, which can increase the electrode/electrolyte contact area and provide more electrochemical reaction sites. The good contact between $FeF_3 \cdot 0.33H_2O$ and GF established by $scCO_2$ can not only provide an efficient medium for lithium ion and electron transport, but also ensure good flexibility of the electrode. The FeF_3@GF–$scCO_2$ electrode demonstrates a capacity of about 145 mA h g^{-1} at a current density of 200 mA g^{-1} and good rate performance. The electrode also shows excellent flexibility, as no structural failure was observed after bending. Further, when assembled into a flexible battery, it was able to power a green light-emitting diode (LED) when bent.

Experimental

Synthesis of graphene foam (GF)

Graphene foam was directly grown on nickel foam (1.65 mm thick, Alantum Advanced Technology Materials, China) under ambient pressure chemical vapor deposition, and the nickel foam was cut into small disks (R = 12 mm). The growth procedure was conducted in a horizontal quartz tube fixed inside a high-temperature furnace (HTF 55322C Lindberg/Blue M). The growth protocol consisted of four steps: (1) the nickel foam was heated to 1000 °C in 30 min under the atmosphere of Ar (500 sccm) and H_2 (50 sccm), and then annealed at 1000 °C for 10 min without changing the gas flow; (2) a nominal amount of CH_4 (5 sccm) was brought into the reaction tube at ambient pressure for 5 min; (3) the samples were cooled to room temperature naturally with Ar (500 sccm). The nickel backbone was etched by using HNO_3 solution (1 M) for 12 h, and then the GF was washed with ultrapure water and ethanol.

Fabrication of FeF_3@GF–$scCO_2$

Iron(III) nitrate nonahydrate absolute ethanol solution (1.55 wt%, 8 mL), 1-butyl-3-methylimidazolium tetrafluoroborate ([Bmim][BF_4]) ionic liquids (3 mL) and GF (~0.4 mg) were loaded into a high-pressure stainless vessel with a volume of 25 mL. Then carbon dioxide was injected by using a high pressure pump to 9.0 MPa at 45 °C. The vessel was put in an oven at 140 °C for 10 h. After the vessel was cooled to room temperature, carbon dioxide and ethanol were removed. The materials were washed with absolute ethanol at least 5 times. Then the composites were dried in a vacuum oven at 60 °C for 2 h. The control experiments were conducted under the same conditions except for the injection of high-pressure CO_2.

Characterization

Raman spectroscopy was performed with a laser micro-Raman spectrometer (Renishaw in Via, Renishaw, 532 nm excitation wavelength). Scanning electron microscopy (SEM) images were obtained by using a ZEISS Merlin Compact and the Energy Dispersive X-ray Spectroscopy (EDX) images were obtained by using an INCAPentalFETx3 Oxford EDX. The XPS measurements were conducted with a Thermo Scientific, ESCALAB 250Xi. The measuring spot size was 500 μm and the binding energies were calibrated by referencing the C 1s peak (284.6 eV). X-Ray diffraction (XRD) measurements were performed with a LabX XRD-6000 using Cu-Kα radiation over the range of 2θ = 10–60°. All the weights were obtained by using an Analytical balance (METTLER TOLEDO, MS-105DU).

Electrochemical measurements

Electrochemical measurements were conducted in standard CR2016 cells. The cells were assembled in an Ar-filled glovebox by directly using the as-prepared FeF_3@GF–$scCO_2$ as the working electrode without adding any binder or conductive agents and lithium metal circular foil (1.5 mm) as the counter electrode. The electrolyte used was 1.0 M $LiPF_6$ in ethylene carbonate and diethyl carbonate (EC/DEC, 1 : 1 by volume). Galvanostatic charge–discharge tests were conducted at various current densities in the voltage range from 1.4 V to 4.5 V with a multichannel battery tester (LAND CT 2001A, Wuhan LAND Electronics CO., Ltd). All of the specific capacities were calculated on the basis of the weight of $FeF_3 \cdot 0.33H_2O$. The mass of the entire electrodes and $FeF_3 \cdot 0.33H_2O$ is shown in Table S1.† The cyclic voltammetry (CV) tests were performed using an electrochemical workstation (CHI610E, Chenhua, Shanghai) at a sweeping rate of 0.2 mV s^{-1} with the voltage ranging from 1.4 V to 4.5 V. Electrochemical impedance spectroscopy (EIS) spectra were measured in the frequency range from 100 KHz to 0.1 Hz on a electrochemical workstation (Im6e, Zahner). For the flexible battery, the FeF_3@GF–$scCO_2$ electrodes and the lithium metal electrodes were encapsulated by silica gel.

Results and discussion

The Raman spectra of GF and FeF_3@GF–$scCO_2$ are presented in Fig. 1a. In the Raman spectra of FeF_3@GF–$scCO_2$, the small D peak at 1350 cm^{-1} indicates that only few defects are introduced into the GF (I_D/I_G = 0.062) during the synthesis process.[33] The small disorder-induced D band indicates the high quality of the GF, which makes it appropriate to serve as a high conductivity framework to improve the electrical conductivity of the FeF_3@GF–$scCO_2$ electrode.[31,34] In addition, the intensity of the G band is higher than that of the 2D band, which is consistent with the multilayer properties of graphene foam.[33] The obtained Fe_3O_4@GF–$scCO_2$ was characterized by X-ray diffraction (XRD) (Fig. 1b). The two typical diffraction peaks centered at 26.5° and 54.6° are attributed to the (002) and (004) reflections of graphitic carbon, respectively (JCPDS card 75-1621).[31] There are another five peaks appearing in the composites, which are

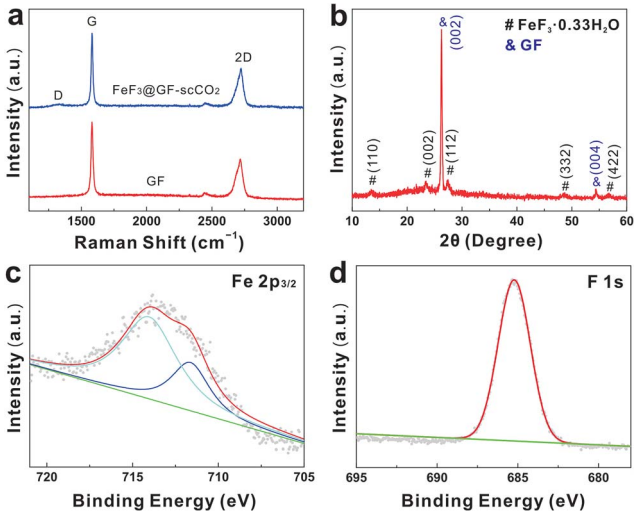

Fig. 1 (a) Raman spectra of GF and FeF_3@GF–$scCO_2$. (b) X-ray diffraction patterns of FeF_3@GF–$scCO_2$. (c and d) X-ray photoelectron spectra of FeF_3@GF–$scCO_2$, in which (c) corresponds to the Fe $2p_{3/2}$ states and (d) corresponds to F 1s states.

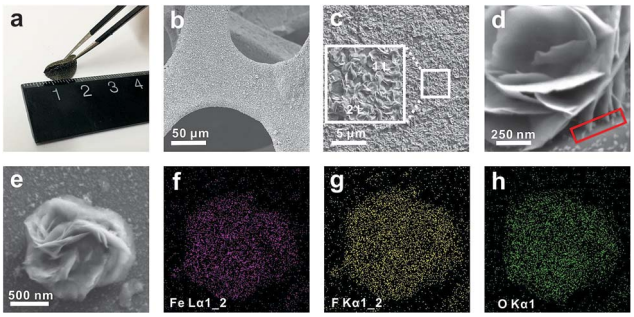

Fig. 2 (a) Photograph of free-standing flexible FeF_3@GF–$scCO_2$ being bent (R = 0.6 cm). (b) Low-magnification SEM image of FeF_3@GF–$scCO_2$ (c) the representative enlarged morphology image of FeF_3@GF–$scCO_2$. The inset shows the 1 layer (1 L) and 2 layers (2 L) of $FeF_3 \cdot 0.33H_2O$ microflowers. (d) SEM image of the side view of a single microflower grown on GF. The red rectangle shows the interface between $FeF_3 \cdot 0.33H_2O$ and GF. (e) SEM image of the top view of another microflower grown on GF; corresponding elemental mapping images of (f) Fe, (g) F and (h) O.

attributed to the (110), (002), (112), (332) and (422) reflections of $FeF_3 \cdot 0.33H_2O$ (JCPDS card 76-1262).[26] In order to further confirm the XRD results, the oxidation states and composition of iron fluorides were examined by X-ray photoelectron spectroscopy (XPS). The XPS spectrum of the FeF_3@GF–$scCO_2$ sample is illustrated in Fig. S1a.† It is clear that the signals of Fe, F, O and C appear on the spectrum. Fig. S1b† shows the high resolution XPS spectra of C 1s. The oxidized carbon species (C–O, centered at 286.3 eV)[35] is attributed to the bond between GF and $FeF_3 \cdot 0.33H_2O$, which confirms the strong contact between GF and $FeF_3 \cdot 0.33H_2O$. Fig. 1c shows one peak at 713.9 eV, which suggests the +3 oxidation state of iron in the material, which matches previous reports for FeF_3.[36] The smaller peak located at 711.3 eV corresponds to the +2 oxidation state of iron, indicating the small amount of FeF_2 in this material.[37] The absence of a reflection that corresponds to FeF_2 in the XRD results also substantiates this. The binding energy for the F 1s level measured from Fig. 1d was 685.2 eV, which closely matches those of metal fluorides.[38] By analyzing the results of XRD and XPS, the presence of $FeF_3 \cdot 0.33H_2O$ NPs can be confirmed.

Fig. 2a shows a photograph of the FeF_3@GF–$scCO_2$ composite being bent without breaking, demonstrating the good flexibility of this material. Moreover, the low-magnification SEM image of FeF_3@GF–$scCO_2$ (Fig. 2b) shows that the 3D network is similar to GF (Fig. S2a and b†). Fig. 2b and c show that the $FeF_3 \cdot 0.33H_2O$ microflowers obtained by our $scCO_2$ process grow on GF homogeneously within 1–2 layers. The few-layer $FeF_3 \cdot 0.33H_2O$ grown on GF has no effect on the electrical conductivity of the GF. To validate the pivotal effect of a $scCO_2$ medium, we performed a controlled experiment for comparison. GF was soaked in iron nitrate ethanol solution under the same conditions but without $scCO_2$ (denoted as FeF_3@GF–HT). Fig. S2c and d† demonstrate that the multilayer microflowers weakly anchored on GF are prone to agglomerate, leading to incomplete utilization of active materials ($FeF_3 \cdot 0.33H_2O$). Moreover, the inhomogeneous distribution of $FeF_3 \cdot 0.33H_2O$ will affect the electrical conductivity of the electrode seriously. Fig. 2d shows the SEM image of the side view of a single microflower grown on GF. As can be seen from the image, $FeF_3 \cdot 0.33H_2O$ microflowers grow on GF with many nanopetals standing perpendicular to the surface of the GF. The good contact (see the red rectangle in Fig. 2d) between $FeF_3 \cdot 0.33H_2O$ and GF was obtained by the $scCO_2$ method, which has the properties of low viscosity, rapid diffusivity, and absence of surface tension. This structure not only provides a large interfacial area for fast lithium insertion/extraction but also ensures a short solid-state diffusion length.[16] Fig. 2e shows a SEM image of the top view of another microflower grown on GF. Fig. 2f–h correspond to the elemental mapping images of (f) Fe, (g) F and (h) O, which suggest the presence of the elements C, F, and Fe in the composites and the homogeneous distribution of these three components. The TEM-EDX spectrum (Fig. S3†) of the composites also confirms the presence of Fe, F, O and C, demonstrating that no precursors are left.

Fig. 3a shows a representative transmission electron microscopy (TEM) evaluation of parts of nanopetals of $FeF_3 \cdot 0.33H_2O$ microflowers synthesized by $scCO_2$. The $FeF_3 \cdot 0.33H_2O$ nanopetals consist of $FeF_3 \cdot 0.33H_2O$ NPs, which were uniformly distributed and well adhered on the graphene sheets (Fig. 3b). Furthermore, the selected area electron diffraction (SAED) analysis (inset of Fig. 3b) proves the polycrystalline nature of $FeF_3 \cdot 0.33H_2O$. The NPs have a narrow size distribution of 15 ± 5 nm, as shown in Fig. 3d. The HRTEM image of $FeF_3 \cdot 0.33H_2O$ and GF is shown in Fig. 3c. The lattice fringes with a d-spacing of 0.293 nm can be assigned to (041) planes of the $FeF_3 \cdot 0.33H_2O$ crystal. The lattice fringes with a d-spacing of 0.169 nm can be assigned to (004) planes of the graphene crystal. Besides, the good contact between $FeF_3 \cdot 0.33H_2O$ and GF can be confirmed by using the HRTEM image as the two components are adjacent to each other.

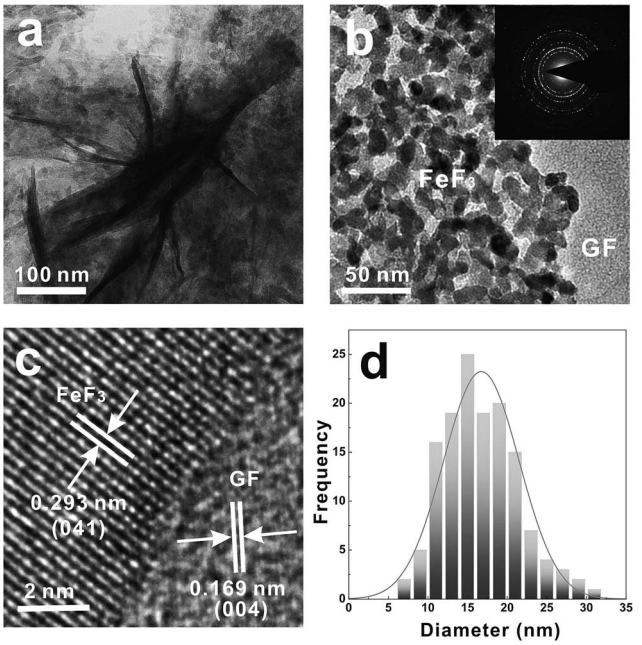

Fig. 3 (a) TEM image of the nanopetals of $FeF_3 \cdot 0.33H_2O$ microflowers (b) enlarged TEM image of the nanopetals and GF and the inset shows the corresponding SAED patterns. (c) HRTEM image of an individual $FeF_3 \cdot 0.33H_2O$ and GF. (d) The size distribution of $FeF_3 \cdot 0.33H_2O$ NPs which fabricated the nanopetals.

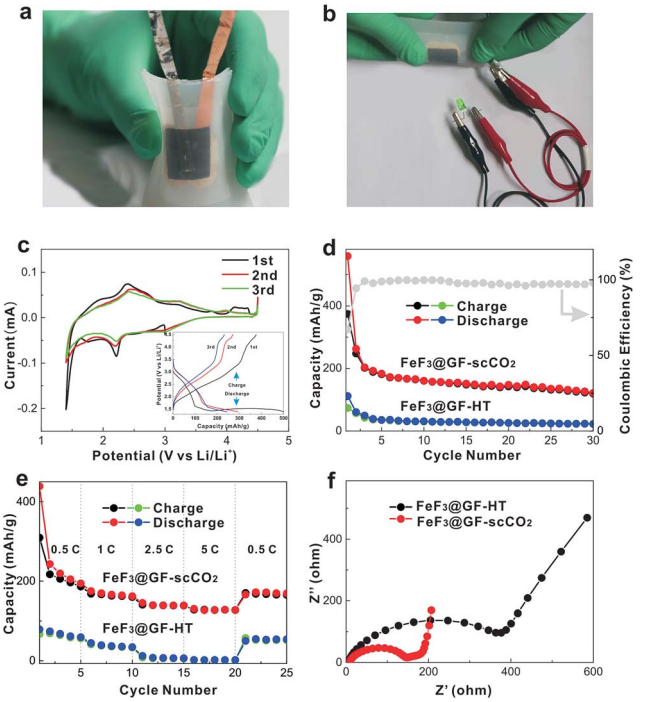

Fig. 4 (a) Photograph of a bent battery encapsulated by silica gel, showing its good flexibility. (b) Lighting a green LED device under bending. (c) CV curves of the FeF_3@GF–$scCO_2$ electrode at a sweeping rate of 0.2 mV s^{-1} with the range from 1.4 to 4.5 V. The inset shows the corresponding charge/discharge voltage profiles. (d) Cycling performance of Fe_3O_4@GF–$scCO_2$ and FeF_3@GF–HT at 1C (200 mA g^{-1}) rate. (e) Rate performance of the FeF_3@GF–$scCO_2$ electrode and FeF_3@GF–HT electrode. (f) EIS of the FeF_3@GF–$scCO_2$ and FeF_3@GF–HT electrodes.

To determine the flexible performance of the FeF_3@GF–$scCO_2$ electrodes, the electrodes and lithium metal electrodes were encapsulated by silica gel to assemble the battery. Due to the small thickness and great flexibility of the GF-based electrodes (Fig. 2a), the battery shows excellent flexibility, and no structural failure was observed after bending (Fig. 4a). This flexible battery is able to power a green light-emitting diode (LED) when bent, as shown in Fig. 4b. Fig. S4† shows the photographs of lighting a green LED device under various bending radii and directions, which demonstrate the good flexibility of the battery. To determine the electrochemical performance of the FeF_3@GF–$scCO_2$ electrodes, they were assembled into coin cells with lithium foils as reference electrodes. The lithium storage behavior was characterized by cyclic voltammetry. As shown in Fig. 4c, in the cathodic process of the first cycle, three well-defined reduction peaks can be observed at 3.00 V, 2.22 V and 1.5 V. The peak located at 3.00 V and 2.22 V corresponds to the structure transition caused by the insertion of lithium-ions into FeF_3 ($Fe^{3+}F_3 + Li^+ + e^- \rightarrow Li\ Fe^{2+}F_3$), as the cutoff voltage of the reaction is approximately 2 V.[39] And the peaks centered at 1.5 V correspond to the further transformation of $LiFeF_3$ to Fe^0 and LiF by a conversion reaction [$Li\ Fe^{2+}F_3 + 2\ Li^+ + 2\ e^- \rightarrow 3LiF + 3Fe^0$].[40] During the anodic process of the first cycle, it is clear that there are three oxidization peaks at approximately 2.38, 3.20 and 3.76 V. The first two peaks correspond to the inverse reaction of the two reactions mentioned above, while the third one may arise from the deintercalation of $Li_{0.5}FeF_3$.[41] The broad reduction peak located between 4.1 and 4.3 V corresponds to the formation of SEI, which cannot be observed in the second and third cycle. The subsequent cycles show good reproducibility, in which the cathodic lithium insertion mainly occurs at 3.00 V and 2.22 V, whereas the anodic lithium extraction occurs at 2.42 V and 3.26 V due to a two-step reversible reaction and the peaks at 3.97 V may arise from the deintercalation of $Li_{0.5}FeF_3$.[36] The charge/discharge voltage profiles of FeF_3@GF–$scCO_2$ shown in the inset of Fig. 4c also confirm the electrochemical reaction. To elaborate the advantages of employing $scCO_2$ over cycling stability, we conducted controlled experiments to offer comparisons. Discharge–charge measurements were performed at 1C (200 mA g^{-1}) rate for 30 cycles under ambient conditions. As shown in Fig. 4d, the capacity of the FeF_3@GF–$scCO_2$ electrode decreases to 170 mA h g^{-1} in the initial 10 cycles, and the capacity still remains at about 145 mA h g^{-1}after 30 cycles, whereas the capacity of the FeF_3@GF–HT electrode drops off significantly to ~30 mA h g^{-1} in the initial 10 cycles and then decreases to ~20 mA h g^{-1} at the subsequent 20 cycles. The capacity of the FeF_3@GF–$scCO_2$ electrode obviously demonstrates its excellent electrochemical performance over FeF_3@GF–HT. The good cycling stability of FeF_3@GF–$scCO_2$ benefits from the strong contact between FeF_3 and GF, which can be easily achieved by the $scCO_2$ method.[31] The charge/discharge curve of GF (Fig. S5†) shows a potential plateau at about 0.2 V, which demonstrates that the high-voltage window (1.4–4.5 V) prevents lithium-ion intercalation in GF.[16] The rate performance of these two

electrodes further confirmed the advantages of our $scCO_2$ method. As can be seen from Fig. 4e, FeF_3@GF–$scCO_2$ shows superior rate performance with capacities of 200 mA h g^{-1} at 0.5C, 170 mA h g^{-1} at 1C, 140 mA h g^{-1} at 2.5C and 130 mA h g^{-1} at 5C. Moreover, the capacity still remains as high as 170 mA h g^{-1} when the C rate returns back from 5C to 0.5C, indicating its high stability and excellent reversibility. In sharp contrast, the capacity of FeF_3@GF–HT electrodes is less than 10 mA h g^{-1} at 2.5C. To understand the reasons for the excellent electrochemical performance of FeF_3@GF–$scCO_2$, electrochemical impedance spectroscopy (EIS) measurements were carried out. Fig. 4f clearly demonstrates the superior conductivity of the FeF_3@GF–$scCO_2$ electrode over the FeF_3@GF–HT electrode before cycling, which further confirms the SEM results (Fig. 2b and c, S2c and d†).

The FeF_3@GF–$scCO_2$ electrodes show the excellent properties of high specific capacity and good rate performance, which can be ascribed to the following four reasons. First, GF acts not only as a 3D skeleton for $FeF_3 \cdot 0.33H_2O$, but also as a conductive matrix for the composite. The high quality of CVD grown graphene and the less defect-induced $FeF_3 \cdot 0.33H_2O$ synthesis process guarantee a high electrical conductivity of the composites. In addition, a strong contact between the $FeF_3 \cdot 0.33H_2O$ microflowers and the GF is established by our $scCO_2$ process. The excellent conductivity of graphene and good contact shorten the pathways for electrons and provide a fast transport channel for a high Li^+ flux between the electrolyte, $FeF_3 \cdot 0.33H_2O$ and GF, which provide the electrodes with a great potential for fast charging and discharging. Second, the composites with the robust 3D structure of the GF matrix and the flower-like structure of $FeF_3 \cdot 0.33H_2O$ having a large specific surface area increase the electrode/electrolyte contact area, and provide more sites for the electrochemical reaction. Third, the homogeneously distributed nanopetals and the porous hierarchical structure shorten the transport path of ions and electrons, lowering the charge transfer resistance and promoting electrolyte diffusion. Fourth, the nanoparticle composed nanopetals of the microflowers have a narrow distribution (15 ± 5 nm in diameter), which will significantly reduce the strain during the lithiation and delithiation process, thus preserving the structural integrity of the electrode.

Conclusions

In summary, we have developed a $scCO_2$ assisted one-step strategy to fabricate a flexible FeF_3@GF–$scCO_2$ electrode. The flower-like $FeF_3 \cdot 0.33H_2O$ forms many nanopetals uniformly distributed and closely attached to the GF. The designed 3D structure can provide many electrochemical reaction sites. The pores between nanopetals and in GF networks can increase the electrode/electrolyte contact and shorten the transport path of ions and electrons. The reversible specific capacity of our FeF_3@GF–$scCO_2$ electrodes reached 145 mA h g^{-1} at 1C rate after 30 cycles. This binder-free flexible electrode also shows great rate performance up to 130 mA h g^{-1} at 5C rate. The significant improvement in flexible LIB performance and simplicity of using $scCO_2$ will greatly promote the research and applications for flexible energy devices.

Acknowledgements

The research was supported by the Natural Science Foundation of China (Grants 51322209, 21473124), the Sino-German Center for Research Promotion (Grants GZ 871) and the Ministry of Education (Grants 20120141110030).

Notes and references

1 L. Li, Z. Wu, S. Yuan and X. B. Zhang, *Energy Environ. Sci.*, 2014, **7**, 2101.
2 X. L. Wang and G. Q. Shi, *Energy Environ. Sci.*, 2015, **8**, 790.
3 G. M. Zhou, F. Li and H. M. Cheng, *Energy Environ. Sci.*, 2014, **7**, 1307.
4 G. H. Gelinck, H. E. Huitema, E. van Veenendaal, E. Cantatore, L. Schrijnemakers, J. B. van der Putten, T. C. Geuns, M. Beenhakkers, J. B. Giesbers, B. H. Huisman, E. J. Meijer, E. M. Benito, F. J. Touwslager, A. W. Marsman, B. J. van Rens and D. M. de Leeuw, *Nat. Mater.*, 2004, **3**, 106.
5 J. A. Rogers, Z. N. Bao, K. Baldwin, A. Dodabalapur, B. Crone, V. R. Raju, V. Kuck, H. Katz, K. Amundson, J. Ewing and P. Drzaic, *Proc. Natl. Acad. Sci. U. S. A.*, 2001, **98**, 4835.
6 S. K. Bae, H. Kim, Y. B. Lee, X. F. Xu, J. S. Park, Y. Zheng, J. Balakrishnan, T. Lei, H. R. Kim, Y. I. Song, Y. J. Kim, K. S. Kim, B. Ozyilmaz, J. H. Ahn, B. H. Hong and S. Iijima, *Nat. Nanotechnol.*, 2010, **5**, 574.
7 D. H. Kim, J. Viventi, J. J. Amsden, J. Xiao, L. Vigeland, Y. S. Kim, J. A. Blanco, B. Panilaitis, E. S. Frechette, D. Contreras, D. L. Kaplan, F. G. Omenetto, Y. Huang, K. C. Hwang, M. R. Zakin, B. Litt and J. A. Rogers, *Nat. Mater.*, 2010, **9**, 511.
8 H. Ko, R. Kapadia, K. Takei, T. Takahashi, X. B. Zhang and A. Javey, *Nanotechnology*, 2012, **23**, 344001.
9 H. Nishide and K. Oyaizu, *Science*, 2008, **319**, 737.
10 S. Park, M. Vosguerichian and Z. N. Bao, *Nanoscale*, 2013, **5**, 1727.
11 M. Armand and J. M. Tarascon, *Nature*, 2008, **451**, 652.
12 J. M. Tarascon and M. Armand, *Nature*, 2001, **414**, 359.
13 W. H. Cai, T. Lai, W. L. Dai and J. S. Ye, *J. Power Sources*, 2014, **255**, 170.
14 S. Das, P. Sudhagar, Y. S. Kang and W. Choi, *J. Mater. Res.*, 2014, **29**, 299.
15 H. Y. Wang, G. M. Wang, Y. C. Ling, F. Qian, Y. Song, X. H. Lu, S. W. Chen, Y. X. Tong and Y. Li, *Nanoscale*, 2013, **5**, 10283.
16 N. Li, Z. Chen, W. Ren, F. Li and H. M. Cheng, *Proc. Natl. Acad. Sci. U. S. A.*, 2012, **109**, 17360.
17 C. G. Lee, X. D. Wei, J. W. Kysar and J. Hone, *Science*, 2008, **321**, 385.
18 A. Abouimrane, O. C. Compton, K. Amine and S. T. Nguyen, *J. Phys. Chem. C*, 2010, **114**, 12800.
19 H. Gwon, H. S. Kim, K. U. Lee, D. H. Seo, Y. C. Park, Y. S. Lee, B. T. Ahn and K. Kang, *Energy Environ. Sci.*, 2011, **4**, 1277.

20 W. Y. Zhang, J. X. Zhu, H. X. Ang, Y. Zeng, N. Xiao, Y. B. Gao, W. L. Liu, H. H. Hng and Q. Y. Yan, *Nanoscale*, 2013, **5**, 9651.
21 X. H. Cao, B. Zheng, X. H. Rui, W. H. Shi, Q. Y. Yan and H. Zhang, *Angew. Chem., Int. Ed.*, 2014, **53**, 1404.
22 L. F. Cui, L. B. Hu, J. W. Choi and Y. Cui, *ACS Nano*, 2010, **4**, 3671.
23 L. B. Hu, J. W. Choi, Y. Yang, S. Jeong, F. La Mantia, L. F. Cui and Y. Cui, *Proc. Natl. Acad. Sci. U. S. A.*, 2009, **106**, 21490.
24 F. Badway, F. Cosandey, N. Pereira and G. G. Amatucci, *J. Electrochem. Soc.*, 2003, **150**, A1318.
25 F. Badway, N. Pereira, F. Cosandey and G. G. Amatucci, *J. Electrochem. Soc.*, 2003, **150**, A1209.
26 B. J. Li, Z. J. Cheng, N. Q. Zhang and K. N. Sun, *Nano Energy*, 2014, **4**, 7.
27 C. L. Li, X. K. Mu, P. A. van Aken and J. Maier, *Adv. Energy Mater.*, 2013, **3**, 113.
28 L. S. Li, F. Meng and S. Jin, *Nano Lett.*, 2012, **12**, 6030.
29 Y. Lu, Z. Y. Wen, J. Jin, X. W. Wu and K. Rui, *Chem. Commun.*, 2014, **50**, 6487.
30 Y. Lu, Z. Y. Wen, J. Jin, K. Rui and X. W. Wu, *Phys. Chem. Chem. Phys.*, 2014, **16**, 8556.
31 X. B. Hu, M. H. Ma, M. Q. Zeng, Y. Y. Sun, L. F. Chen, Y. H. Xue, T. Zhang, X. P. Ai, R. G. Mendes, M. H. Rümmeli and L. Fu, *ACS Appl. Mater. Interfaces*, 2014, **6**, 22527.
32 T. Seki, J. D. Grunwaldt and A. Baiker, *Ind. Eng. Chem. Res.*, 2008, **47**, 4561.
33 L. M. Malard, M. A. Pimenta, G. Dresselhaus and M. S. Dresselhaus, *Phys. Rep.*, 2009, **473**, 51.
34 Z. P. Chen, W. C. Ren, L. B. Gao, B. L. Liu, S. F. Pei and H. M. Cheng, *Nat. Mater.*, 2011, **10**, 424.
35 Y. L. Liu, X. Y. Wang, J. Q. Xu, C. Xiao, Y. H. Liu, X. W. Zhang, J. T. Liu and W. H. Huang, *Chem. Sci.*, 2015, **6**, 1853.
36 L. Liu, M. Zhou, L. H. Yi, H. P. Guo, J. L. Tan, H. B. Shu, X. K. Yang, Z. H. Yang and X. Y. Wang, *J. Mater. Chem.*, 2012, **22**, 17539.
37 J. C. Carver and G. K. Schweitzer, *J. Chem. Phys.*, 1972, **57**, 973.
38 A. Hamwi, C. Latouche, V. Marchand, J. Dupuis and R. Benoit, *J. Phys. Chem. Solids*, 1996, **57**, 991.
39 H. J. Tan, H. L. Smith, L. Kim, T. K. Harding, S. C. Jones and B. Fultz, *J. Electrochem. Soc.*, 2014, **161**, A445.
40 D. L. Ma, H. G. Wang, Y. Li, D. Xu, S. Yuan, X. L. Huang, X. B. Zhang and Y. Zhang, *Nano Energy*, 2014, **10**, 295.
41 R. E. Doe, K. A. Persson, Y. S. Meng and G. Ceder, *Chem. Mater.*, 2008, **20**, 5274.